RESEARCH ARTICLE | OCTOBER 08 2012

Scaling of turbulent structures in riblet channels up to $Re_\tau \approx 550$

Ricardo García-Mayoral; Javier Jiménez

Physics of Fluids 24, 105101 (2012)
https://doi.org/10.1063/1.4757669

Scaling of turbulent structures in riblet channels up to $Re_\tau \approx 550$

Ricardo García-Mayoral[1,2,a)] and Javier Jiménez[1]
[1]*School of Aeronautics, Universidad Politécnica de Madrid, 28040 Madrid, Spain*
[2]*Center for Turbulence Research, Stanford University, Stanford, California 94305, USA*

(Received 23 April 2012; accepted 19 September 2012; published online 8 October 2012)

Results of direct numerical simulations of riblet channels at $Re_\tau \approx 550$ are presented and compared with previous results at $Re_\tau \approx 180$. Special attention is given to the scaling of the turbulence phenomena associated to the presence of riblets in the wall, particularly to the length scales and intensities of the coherent spanwise rollers whose appearance has been recently reported. © *2012 American Institute of Physics*. [http://dx.doi.org/10.1063/1.4757669]

I. INTRODUCTION

We consider the turbulent flow in channels with riblet walls. Riblets are two-dimensional roughness elements aligned in the direction of the flow that, at small enough sizes, can reduce friction drag. This drag reduction, usually expressed as the relative decrease of the friction coefficient, $DR = -\Delta c_f/c_{f0}$, can be considered a transitional roughness effect,[1] in the sense that it occurs for riblet sizes at which conventional roughness does not yet exhibit a fully rough behavior. The maximum drag reduction of riblets is achieved as the linear regime, for vanishingly small rib spacings,[2,3] begins to degrade, in the transition between that linear behavior and the fully rough regime. The performance of a given geometry depends primarily on the riblet size expressed in wall units,[4] that is, normalized with the kinematic viscosity ν and the friction velocity u_τ. For a wide variety of experimental riblet geometries,[5] we have recently reported that the size for optimum performance collapses when expressed as the square root of the groove cross-section,[6] $\ell_g^+ = (A_g^+)^{1/2}$, where the $+$ superscript denotes dimensions given in wall units. The optimum size is $\ell_{g,opt}^+ \approx 11$. Furthermore, expressing the performance of riblets as a function of ℓ_g^+ leads to a fairly "universal" drag curve, in which the collapse extends reasonably well to the whole drag-reducing range of sizes. We have found from direct numerical simulations (DNSs) that this collapse is due to the onset of a Kelvin-Helmholtz-like instability, which generates spanwise-elongated structures in the flow near the wall. The additional Reynolds stresses associated to these structures account for the degradation in riblet performance. A simplified stability analysis has identified a "penetration length," which depends only on the riblet geometry, as the determining scale for the onset of the instability. This penetration length can be easily calculated and is roughly proportional to ℓ_g^+, providing, on one hand, theoretical support for the collapse observed experimentally, and a simple tool to predict optimum riblet sizes on the other.

In the present paper, results for riblet channels at $Re_\tau \approx 550$ are presented and compared with our previous results at $Re_\tau \approx 180$.[6] Special emphasis is made on the statistical evidence of the Kelvin-Helmholtz-like instability mentioned above. To our knowledge, no similar set of simulations can be found in the literature. In fact, all previous DNSs with riblets had been conducted at $Re_\tau \approx 180$,[7–12] and even DNSs of other types of roughness at Re_τ of order 500 have only begun to appear in recent years.[13–16] In principle, the modulation with Re_τ should be small in the case of riblets, because they appear to interact only with the near-wall structures,[17,18] so the effect of their presence would be restricted to the buffer layer. However, results of simulations at $Re_\tau \approx 180$

a)Electronic mail: gmayoral@stanford.edu.

should always be treated with care, since for such low Re_τ, the flow is only marginally turbulent. The behavior of the flow variables in the buffer layer at $\mathrm{Re}_\tau \approx 180$ deviates slightly from the trends observed at higher Re_τ.[19] Even more critical is the fact that for the larger riblets, the height of the protrusions h is comparable to the flow thickness δ, which is the half-channel height in our case, and which equates to Re_τ when expressed in wall units. It is widely accepted that, in order for roughness elements not to perturb the whole boundary layer, their height should satisfy $h/\delta \lesssim 0.025$.[1] Else, the flow under consideration would be more representative of flows around obstacles (along riblet grooves in our case), than of turbulent flows over rough walls. Riblets are typically $h^+ \approx 10$–15, so to satisfy the above condition simulations should be run at $\mathrm{Re}_\tau \gtrsim 600$. We have designed the current set of simulations to meet that requirement, albeit marginally for the simulation with largest riblets. The comparison of these DNSs with the ones at $\mathrm{Re}_\tau \approx 180$ provides a much-needed justification for the extrapolation of previous results at low Re_τ to flows of practical interest.

II. NUMERICAL SETUP

Part of the reason for similar simulations not having been conducted before is that the computational cost is higher than for smooth-wall DNSs, since the resolution required for the flow around the riblet crests is even finer than that for the direct simulation of near-wall turbulence. Given the high computational cost, we have conducted simulations for fewer cases than in Ref. 6, selecting them so that they were representative of all the different flow regimes. We have also designed the simulations to closely match ℓ_g^+ values from the set of simulations in Ref. 6, so that direct comparisons could be made. Thus, we have simulated a smooth-wall reference case (0L); one with riblets in the viscous regime (7L), with $\ell_g^+ \approx 7$, one near the optimum performance (13L), $\ell_g^+ \approx 13$, and one well past the viscous breakdown (20L), $\ell_g^+ \approx 20$. Throughout the paper, we will compare the present results with those of the corresponding simulations 0S, 7S, 13S, and 20S from Ref. 6, with roughly the same values for ℓ_g^+, but conducted at $\mathrm{Re}_\tau \approx 180$. We have used the same numerical code, a pseudo-spectral, multi-block, immersed-boundary, fractional-step, constant-flow-rate, Runge-Kutta Navier-Stokes solver that enforces incompressibility in a weak sense. The multi-block arrangement was chosen to save computational time. The resolution in the center of the channel is that required for the DNS of turbulence, while the blocks containing the riblet walls have finer resolutions. Further details of the code can be found in Refs. 6 and 20.

The parameters of the simulations are summarized in Table I, including for reference those of the corresponding simulations from Ref. 6. The value of the kinematic viscosity, $\nu = 1/11180$, was chosen so that with the prescribed constant flow rate, the resulting friction Reynolds number was $\mathrm{Re}_\tau \approx 550$. The riblet geometry is the same of Ref. 6, rectangular blades with height-to-spacing ratio $h/s = 0.5$ and tip width $t_r = 0.25\,s$. Assigning a fixed number of 24 collocation points per riblet in

TABLE I. Parameters of the DNSs. N_R is the number of riblets in the simulation box, L_x and L_z are the channel length and width, N_x is the number of collocation points in the streamwise direction, N_{z_c} and N_{z_r} are those in the spanwise direction for the central and wall blocks, respectively, and N_y those in the wall normal direction for $-\delta \le y \le \delta$. T is the approximate total time of the simulation, given in terms of the largest-eddy-turnover time, δ/u_τ. ℓ_g^+ is the square root of the cross-section of the riblet groove, and s^+ the peak-to-peak spacing; $\mathrm{Re}_\tau = \delta^+$ is the friction Reynolds number; c_f is the friction coefficient; and DR is the drag reduction.

Case	N_R	L_x	L_z	N_x	N_{z_c}	N_{z_r}	N_y	Tu_τ/δ	ℓ_g^+	s^+	Re_τ	$c_f \times 10^3$	$DR(\%)$
0L	0	3π	1.50π	576	576	576	453	90	0	0	558.7	4.53	0
07L	216	3π	1.48π	576	576	5184	453	40	7.18	11.73	545.1	4.33	4.50
13L	128	3π	1.52π	576	576	3072	453	40	12.43	20.30	543.6	4.33	4.45
20L	72	3π	1.34π	576	576	1728	453	40	20.39	33.30	568.3	4.67	−3.05
0S	0	2π	0.67π	192	192	192	153	175	0	0	189.3	5.99	0
7S	32	2π	0.67π	192	192	768	153	170	7.39	12.06	184.3	5.76	3.91
13S	18	2π	0.67π	192	192	432	153	169	13.04	21.29	183.0	5.72	4.54
20S	12	2π	0.67π	192	192	288	153	177	20.46	33.41	191.4	6.20	−3.43

the spanwise direction z, the width of the box L_z and the number of riblets N_R are adjusted to obtain approximately the desired ℓ_g^+ values, while keeping the box size larger than the minimal box for the Re_τ considered.[21] For this set of simulations, in the three blocks the number of streamwise x modes was set so that $\Delta x^+ \approx 9$, in terms of collocation points. The spanwise resolution in the central block was set to $\Delta z^+ \approx 4$, while in the fine-resolution blocks, it was determined by N_R and L_z. Depending on the case, the spanwise resolution was thus between 3 and 9 times finer in the wall blocks than in the central one. In the wall-normal direction, $\Delta y^+_{\mathrm{min}} \approx 0.3$ near the riblet peaks, and $\Delta y^+_{\mathrm{max}} \approx 3$ at the center of the channel. The convective and viscous Courant-Friedrichs-Lewy (CFL) numbers, as defined in Ref. 6, were set to $\mathrm{CFL}_C = 0.7$ and $\mathrm{CFL}_V = 2.5$, respectively. Under these conditions, The simulations were run for approximately 40 eddy turn-over times δ/u_τ, of which the first few were discarded to avoid spurious effects of the initial transients on the statistics. The simulation time for case 0L was longer, approximately $90\delta/u_\tau$ because the initial field was taken from case 0S at $\mathrm{Re}_\tau \approx 180$, and the large scales of the flow required very long times to reach equilibrium at the new conditions. In this case, roughly the first half of the simulation was discarded.

III. WALL-FRICTION REDUCTION

Riblet drag curves depend on the Reynolds number mainly through the wall-unit normalization of the riblet size, ℓ_g^+. However, there is an additional, though weak, dependence through the friction coefficient of the reference smooth wall, c_{f0}, which varies slowly with Re.[22] According to the classical theory of wall turbulence, surface manipulations modify the intercept of the logarithmic velocity profile, by an offset ΔB,[23] which is related to DR by

$$DR = \frac{-\Delta B}{(2c_{f0})^{-1/2} + (2\kappa)^{-1}}. \tag{1}$$

Since ΔB is Reynolds-number-independent, the theory indicates that this offset is the quantity to use to reduce experimental results at different Reynolds numbers.[24] Alternatively, the above-mentioned Reynolds number dependence can be eliminated by reducing DR curves with their viscous slopes,[25] which according to Eq. (1) should satisfy

$$m_\ell = \frac{\mu_0}{(2c_{f0})^{-1/2} + (2\kappa)^{-1}} \frac{\Delta h}{\ell_g}, \tag{2}$$

where μ_0 is a universal constant, for which the approximate values of 0.66 (Ref. 26) and 0.78 (Ref. 5) have been given, and Δh is the "protrusion" height,[2] which depends solely on the riblet geometry and can be easily calculated.

The drag reduction results of the present simulations are portrayed in Figure 1, together with the results at $\mathrm{Re}_\tau \approx 180$ from Ref. 6, and the envelope of experimental results for several riblet geometries from Ref. 5. Results are given in terms of DR and DR/m_ℓ. For DNS results, m_ℓ is

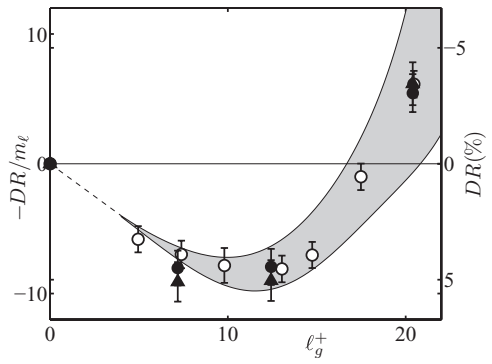

FIG. 1. Friction-reduction for DNSs of channels with rectangular riblets at $\mathrm{Re}_\tau \approx 180$ and 550. ○, DR, and DR/m_ℓ at $\mathrm{Re}_\tau \approx 180$ from Ref. 6; ●, DR at $\mathrm{Re}_\tau \approx 550$; ▲, DR/m_ℓ at $\mathrm{Re}_\tau \approx 550$. Error bars have been estimated from the time-history of c_f.[6,27] The shaded area envelopes results for several experimental riblets.[5]

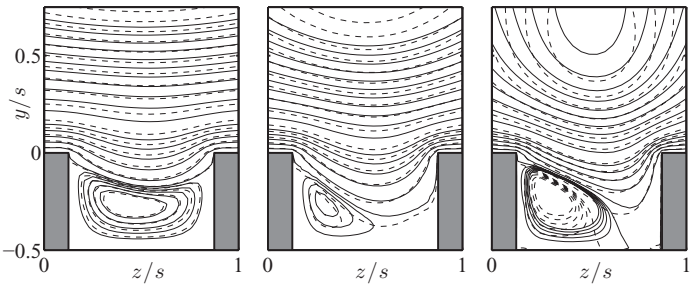

FIG. 2. Streamfunction of the mean crossflow above and within the riblet grooves, conditioned to the presence of a mean rightwards flow in the plane immediately above the riblet tips. From left to right, $\ell_g^+ \approx 7$, $\ell_g^+ \approx 13$, and $\ell_g^+ \approx 20$. To enhance the comparison between the different cases, the streamfunction has been scaled for each case with the corresponding u_τ and riblet height h. —, results from the present simulations at $\mathrm{Re}_\tau \approx 550$, cases 7L, 13L, and 20L. —-, results from the cases 7S, 13S, and 20S of Ref. 6, at $\mathrm{Re}_\tau \approx 180$. The contour levels are $0.05 \times [0(0.2)1]^2$ and 0.10(0.05)0.60 for the rightwards overlying flow, and $-2 \times [0.2(0.2)1] \times 10^{-3}$ for the clockwise recirculation flow.

calculated using Eq. (2), with c_{f0} taken from the reference smooth-wall simulation at roughly the same Re_τ, and the Δh value already calculated for Ref. 6. For experimental riblets, m_ℓ is estimated from the available measurements in the viscous regime. According to Eq. (1), the expected drop in DR from $\mathrm{Re}_\tau \approx 180$ to $\mathrm{Re}_\tau \approx 550$ should be roughly $DR_{550} \approx 0.85\, DR_{180}$, while ΔB, or the analogue DR/m_ℓ, remains essentially unaltered. However, this theoretical prediction cannot be confirmed by the present results, since the expected drop in DR is too small to be distinguished from the statistical uncertainty derived from our finite sampling times.

IV. THE CONDITIONAL FLOW

Following the procedure described in Ref. 6, we have compiled statistics of the flow near the ribbed surface, conditioned both on the y-z position relative to the nearest groove and on the mean direction of the crossflow in the plane immediately above the riblet tips. The crossflow at identical y-z locations with respect to each riblet is averaged over the streamwise direction, time, and the different riblets, but, since that procedure only recovers a weak secondary flow, the statistics are conditioned on the mean direction of the crossflow in the plane immediately above the riblet tips. The flow above each groove section is characterized as either "rightwards" or "leftwards," and the statistics for the two directions are combined by adding the specular image of the mean leftwards flow to the rightwards one. This conditioning generates "mean" flow fields that characterize the cross-plane flow in the riblet groove. The conditioned mean crossflows are portrayed in Figure 2 for simulations 7L, 13L, and 20L, compared with the corresponding simulations at $\mathrm{Re}_\tau \approx 180$ from Ref. 6. In agreement with the latter, the figure shows that there is a weak recirculation bubble in the riblet groove, which becomes increasingly asymmetric for the larger riblets. The streamlines immediately above the riblet peaks, which separate the recirculation regions from the overlying flow, follow nearly the same trajectories, for each ℓ_g^+, at $\mathrm{Re}_\tau \approx 180$ and 550.

On the other hand, as ℓ_g^+ increases, the size of the grooves becomes comparable to that of the overlying quasi-streamwise vortices and, as discussed in Ref. 6, the localized presence of the vortices above the grooves becomes increasingly apparent, in the form of curved streamlines. There is some modulation with the Reynolds number at the region dominated by these vortices, $y^+ \approx 10$–20 above the riblet peaks. However, this dependence is likely attributable to the increase in perturbation intensities, particularly in v'^+, also found in smooth-wall turbulence,[19,27,28] and is thus essentially independent of the presence of riblets.

V. KELVIN-HELMHOLTZ ROLLERS

In Ref. 6, we reported that the degradation in riblet performance with increasing ℓ_g^+ was caused by the appearance of spanwise-elongated, roll-like structures in the immediate vicinity of the wall,

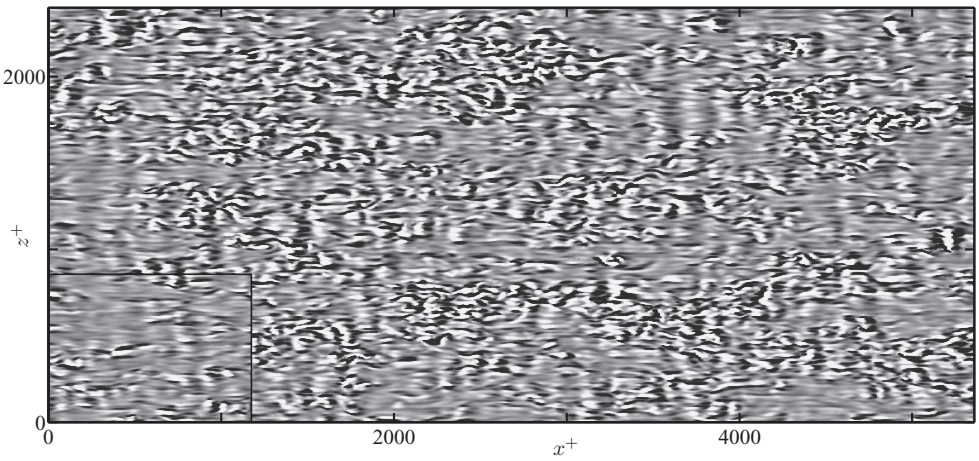

FIG. 3. Instantaneous realizations of the wall-normal velocity at a plane $y^+ \approx 4$, in channels with riblets larger than the optimum and at $\mathrm{Re}_\tau \approx 180$ and 550. The main panel corresponds to an instant of simulation 20L, with $\ell_g^+ \approx 20$ and $\mathrm{Re}_\tau \approx 550$, while the rectangular inset in the lower left corner was obtained from a simulation with $\ell_g^+ \approx 17$ at $\mathrm{Re}_\tau \approx 180$. The dark regions represent negative velocities, or flow towards the wall, with the darkest being $-0.5u_\tau$ and the light regions positive velocities, with the lightest being $0.5u_\tau$.

$y^+ \lesssim 25$, originating from a Kelvin-Helmholtz-like instability of the mean flow. The instability appeared only for riblets larger than the optimum, for which the spanwise structures left a distinct trace in the energy spectrum of the different flow variables. This trace made possible the clear identification of the characteristic length scales of the structures. However, since all the simulations were conducted at a roughly equal Reynolds number, the scaling of the spanwise structures was unclear, and it remained to be determined whether they scaled in wall or outer units.

To help the reader visualize the general appearance of these structures, Figure 3 portrays, at $\mathrm{Re}_\tau \approx 180$ and 550, the instantaneous realizations of the wall-normal velocity at a plane $y^+ \approx 4$ above the peaks of riblets with $\ell_g^+ \approx 17$ and 20, respectively, for which the Kelvin-Helmholtz instability is fully developed. Just above the riblet peaks, their immediate vicinity damps the wall-normal velocity almost completely, generating streamwise-aligned stripes of very low v separated from each other by the riblet spacing. Above the grooves, where v can attain higher values, the rollers can be observed in the form of the spanwise-coherent regions of alternated up and downwash flow. These regions can span a substantial number of riblet grooves, in spite of being disrupted with riblet-spacing periodicity by the low-v regions above the peaks just commented. The realization at $\mathrm{Re}_\tau \approx 180$ was obtained for a slightly smaller riblet spacing, so the spanwise-periodic disruption has a slightly smaller wavelength, but very similar rollers can be observed in both cases, nevertheless.

One noticeable difference between both flows is the presence, for $\mathrm{Re}_\tau \approx 550$, of regions with more intense fluctuations, of roughly $2000\,\nu/u_\tau \times 500\,\nu/u_\tau$ in the streamwise and spanwise directions, although this is a feature common with smooth-wall flows. The intense regions are the footprint of the outer large structures on the near wall region,[29,30] described as "cat paws" by Hunt and Morrison.[31] Their size scales in outer units, and their predicted streamwise-spanwise wavelengths would be of up to $6\,\delta \times 3\,\delta$,[32] which is in reasonable agreement with our observations. Since they modulate the background turbulence, these "cat paws" interact with the spanwise rollers, as with the rest of the turbulent fluctuations, by locally increasing or decreasing their intensity,[30] but are otherwise an independent phenomenon. Because of the limited Re_τ and domain size, this outer-scale effect could not be captured by our previous simulations at $\mathrm{Re}_\tau \approx 180$.

From a statistical perspective, the spanwise rollers can be traced in the spectral distributions of energy density of the different flow variables. A concentration of high values in these distributions at a certain λ_x-λ_z region implies that the structures with those wavelengths carry a significant part of the energy in the flow. We will leave out of our analysis the effect of the modulation of the rms fluctuations with Re_τ but, for reference, they are given in Figure 4 for the three velocity components,

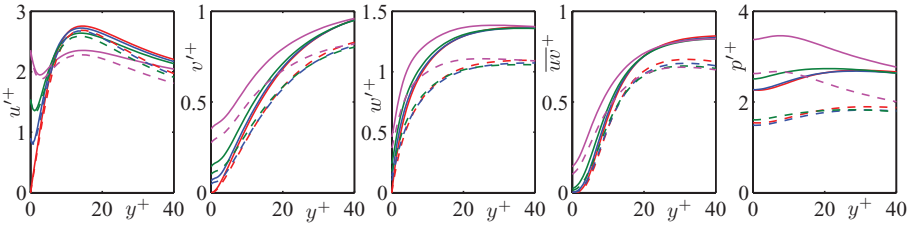

FIG. 4. Root mean square fluctuations of the three velocity components, the Reynolds stress, and the pressure, as a function of ℓ_g^+ and Re_τ. Dashed lines represent $\mathrm{Re}_\tau \approx 180$, and solid ones $\mathrm{Re}_\tau \approx 550$. ℓ_g^+ has values 0, 7, 13, and 20 from lowest to highest fluctuation value at $y^+ = 0$, i.e., red lines are for $\ell_g^+ = 0$, and blue, green and magenta ones for $\ell_g^+ \approx 7$, 13, and 20, respectively.

the Reynolds stress, and the pressure. As mentioned above, the rms fluctuations just above $y^+ = 0$ increase with Re_τ, especially for the wall-normal velocity and the pressure, and similarly in smooth-wall and ribbed channels. There is also a modulation with ℓ_g^+, which has been widely discussed in the literature,[6,7,10,33] although that has not been the case for their spectra. To compare the new results with those at $\mathrm{Re}_\tau \approx 180$ from Ref. 6, while leaving out the effect of the modulation of the rms with Re_τ, the spectral distributions at each y-plane are scaled with the corresponding rms values. Some illustrative results are portrayed in Figure 5, which contains examples of two-dimensional, spectral energy densities over wall-parallel planes at small heights y^+ above the riblet peaks. Additional examples can be found in Ref. 20.

The spanwise rollers leave their trace on the spectra in the region with $\lambda_x^+ \approx 100-200$ and $\lambda_z^+ > 100$, where energy concentrates for riblets larger than the optimum. As at $\mathrm{Re}_\tau \approx 180$, the structures develop only for the larger riblets, and only close to the wall. For the wall-normal velocity and pressure fluctuations, the structures reach up to $y^+ \approx 20$–25, while for the other two velocity components and the Reynolds stress, they are approximately half as tall. As an example, Figures 5 (*a*4) through (*a*8) portray, for $\ell_g^+ \approx 20$ and for the wall-normal velocity, how the intensity of the rollers decreases with increasing y^+, vanishing for $y^+ > 20$. For all the variables, the typical length scales are similar at $\mathrm{Re}_\tau \approx 180$ and 550, but the relative energy contained in the region of the rollers at $\mathrm{Re}_\tau \approx 550$ is somewhat higher, particularly for the intermediate $\ell_g^+ \approx 13$, as shown in Figures (*a*3) and (*b*3). This suggests that the instability begins to appear for smaller ℓ_g^+ than at $\mathrm{Re}_\tau \approx 180$, although the difference is very small. The earlier onset of the instability is probably related to the higher fluctuation levels shown in Figure 4, since it is driven by the background fluctuations, that is, they serve as the initial perturbations from which the instability grows. This shift of the onset towards smaller ℓ_g^+ would evolve even more slowly as Re_τ increases further, since the increase of the mean fluctuations is much larger from the marginally turbulent $\mathrm{Re}_\tau \approx 180$ to 550,[19] than from $\mathrm{Re}_\tau \approx 550$ on.[34]

Our new simulations also allow us to establish an upper bound for the spanwise lengthscale of the rollers. Since the size of the simulation domain is now much larger, $L_x^+ \times L_z^+$ of order 5000 $\times$ 2500 compared to the previous 1000 $\times$ 400, the new spectral densities are not artificially cropped for the higher wavelengths, at least near the wall, which is the region under our scrutiny. Thus, it is now possible to obtain the full spectral distribution of the flow variables, bounding the wavelengths of the new structures. At $\mathrm{Re}_\tau \approx 180$, the rollers could span the full width of the domain, while in our new simulation, a maximum $\lambda_z^+ \approx 1000 - 1500$ can be established, except perhaps for the trace in the spectrum of the pressure. Nevertheless, since $\lambda_z^+ \gg \lambda_x^+$ and $\lambda_z^+ \gg \lambda_y^+$, where $\lambda_y^+ \approx 10-20$ is the typical height of the structures above the riblet peaks, the hypothesis that the structures are elongated in the spanwise direction is confirmed, and the connection to the spanwise-homogeneous Kelvin-Helmholtz instability holds.[6]

The scaling of the spanwise rollers in wall units, instead of outer ones, hypothesized in Ref. 6, can be confirmed from Figure 5, but it can be more clearly appreciated in Figure 6. The latter portrays, for $\ell_g^+ \approx 13$ and 20 and for $\mathrm{Re}_\tau \approx 180$ and 550, the distribution in y and in streamwise wavelengths of the additional energy stored in wall-normal velocity structures in the spectral region of the rollers, taking as reference the corresponding smooth wall. For comparison, these distributions

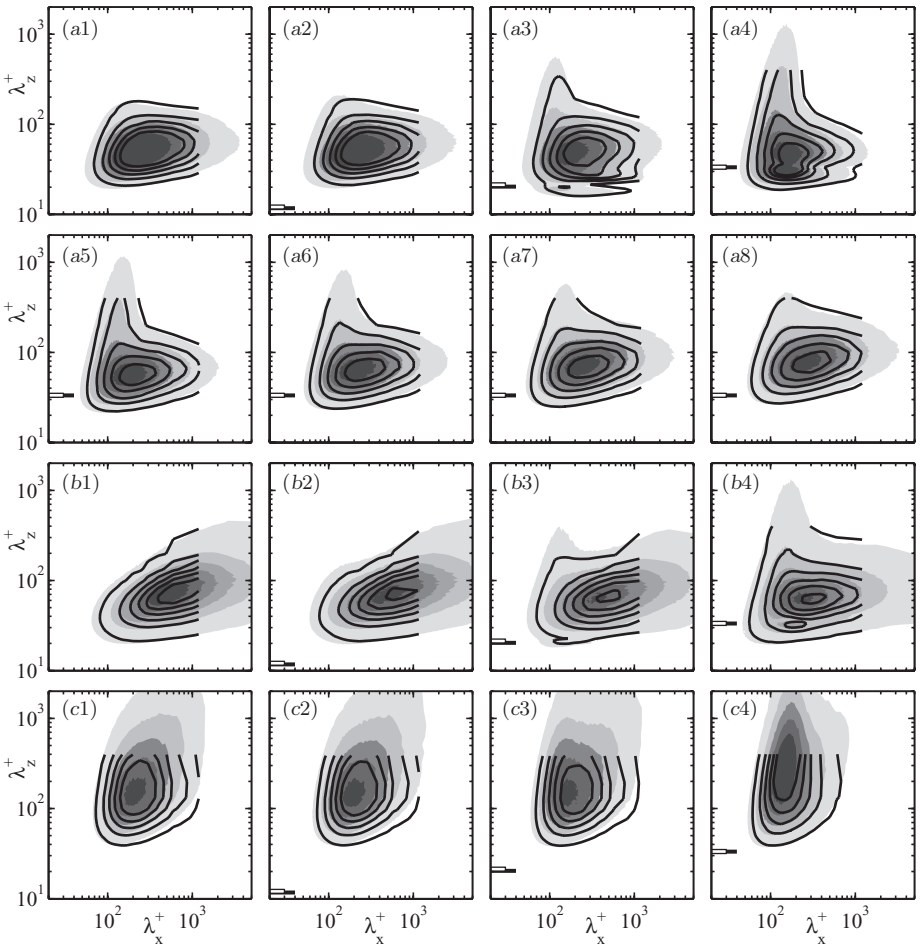

FIG. 5. Spectral energy density of different flow variables. Solid contours are used for $\mathrm{Re}_\tau \approx 180$, and shaded ones for $\mathrm{Re}_\tau \approx 550$. The white and black thick horizontal lines to the left of the plots mark the respective riblet z-wavelengths. (a), premultiplied spectrum of the wall-normal velocity, $k_x k_z E_{vv}$, with contours at $(0.04 : 0.04 : 0.20)\,(v'^+)^2$. ($a1$) through ($a4$), at $y^+ \approx 5$; from left to right, for smooth walls, $\ell_g^+ \approx 7$, 13 and 20. ($a5$) through ($a8$), for $\ell_g^+ \approx 20$; from left to right, at $y^+ \approx 10$, 15, 20, and 25. ($b1$) through ($b4$), premultiplied cospectrum of the Reynolds stress, $-k_x k_z E_{uv}$, at $y^+ \approx 5$, with contours at $(0.01 : 0.05 : 0.26)\,\overline{uv}^+$; from left to right, for smooth walls, $\ell_g^+ \approx 7$, 13, and 20. ($c1$) through ($c4$), premultiplied spectrum of the pressure fluctuations, $k_x k_z E_{pp}$, at $y^+ \approx 10$, with contours at $(0.032 : 0.032 : 0.160)\,(p'^+)^2$; from left to right, for smooth walls, $\ell_g^+ \approx 7$, 13, and 20.

of additional energy are portrayed with the length scales normalized both with the wall unit, ν/u_τ, and the channel half-width δ. The figure shows that the additional spectral densities lie in the same region for the two different Reynolds numbers when using wall scaling, and that they do not when outer units are used. In outer scaling, there is a ratio of roughly three in the length scales, which is what should be expected from the ratio in Re_τ, for structures that scale in wall units.

In Ref. 6, we showed that the spanwise rollers are responsible for the degradation of *DR* past the optimum riblet size. Comparing the momentum balance across channels with smooth and ribbed walls, we derived the following equation:

$$DR \approx \frac{\Delta U_\delta^{+2}}{U_\delta^{+2}} = DR_1 + DR_2 + DR_3, \tag{3}$$

where

$$DR_1 = -\left[1 - \frac{\delta U_\delta}{\delta' U_{\delta S}}\right]\left(\frac{U_{\delta S}^+}{U_\delta^+}\right)^2, \tag{4}$$

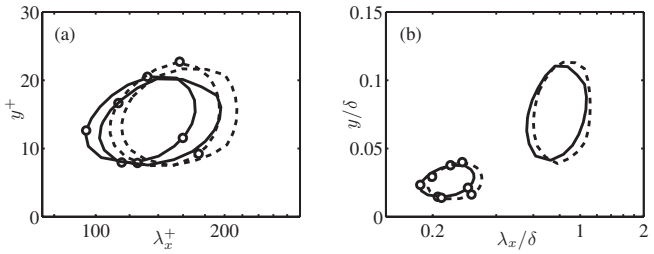

FIG. 6. Increment in the pre-multiplied spectra of the wall-normal velocity caused by the presence of riblets, integrated for $\lambda_z^+ \gtrsim 200$. Lengths are scaled in wall units in (a), and with the channel half-height δ in (b). —, $\ell_g^+ \approx 13$; - - - -, $\ell_g^+ \approx 20$. The contours with open symbols correspond to simulations at $\mathrm{Re}_\tau \approx 180$, and the ones without to $\mathrm{Re}_\tau \approx 550$. The isolines drawn have been chosen to enhance the comparison of the scales in the four cases considered, regardless of their magnitude.

$$DR_2 = \frac{U_0^+}{U_\delta^+}, \tag{5}$$

$$DR_3 = -\frac{\delta\delta^+}{\delta' U_\delta^+} \int_0^1 \left(\tau_{uv}^* - \tau_{uvS}^+\right) \mathrm{d}(y/\delta). \tag{6}$$

In the above equations, the subscript "S" is used to refer to the reference smooth channel; $\delta' = \delta + \mathcal{O}(h)$ is the half-height of the virtual smooth channel that would give the same cross-section as the ribbed channel, in our case $\delta' = \delta + 3h/4$; U_δ and U_0 are, respectively, the mean streamwise velocities at the centerline and riblet-tip planes; τ_{uv} is the Reynolds stress; and the star superscript implies scaling with $u_* = u_\tau(\delta/\delta')^{1/2}$, the friction velocity that would be obtained by extrapolating the linear stress profile within the channel to δ' instead of δ. Using Eq. (1), the three terms can be expressed in terms of the corresponding, Reynolds-number-independent offsets, ΔB_1, ΔB_2, and ΔB_3,

$$\Delta B_i = -\left[(2c_{f0})^{-1/2} + (2\kappa)^{-1}\right] DR_i, \qquad i = 1, 2, 3. \tag{7}$$

Note that at the Reynolds numbers considered, with c_{f0} of order 5×10^{-3}, the factor $[(2c_{f0})^{-1/2} + (2\kappa)^{-1}]$ is of order 10, so that $DR \approx 10\%$ corresponds to $\Delta B \approx 1$. The offsets ΔB_i from our simulations at $\mathrm{Re}_\tau \approx 550$ are portrayed in Figure 7, together with the results at $\mathrm{Re}_\tau \approx 180$ from Ref. 6.

The term ΔB_1 is a correction factor due to the differences in the definition of the channels, both in height and in mass flux. It has no physical meaning, since it merely accounts for the

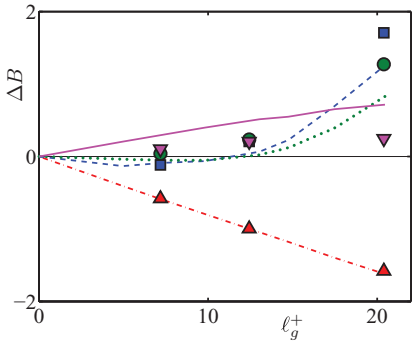

FIG. 7. Contributions ΔB_1, ΔB_2, and ΔB_3 to the reduced drag reduction curve, as defined by Eqs. (4)– (7). Magenta solid line and $\triangledown$, ΔB_1 for $\mathrm{Re}_\tau \approx 180$ and 550, respectively; red chain-dotted line and $\triangle$, ΔB_2 for $\mathrm{Re}_\tau \approx 180$ and 550; blue dashed line and $\square$, ΔB_3 for $\mathrm{Re}_\tau \approx 180$ and 550; green dotted line and $\circ$, ΔB_3 for $\mathrm{Re}_\tau \approx 180$ and 550, integrated only for the spectral region corresponding to the rollers, $65 \le \lambda_x^+ \le 290$, $\lambda_z^+ \ge 50$, and $y^+ \lesssim 35$.

different setups of the smooth and ribbed channels. It follows from its definition that it should vanish for high Re_τ as $10 \times \mathcal{O}(h/\delta)$. Thus, it can be considered a low-Reynolds number artifact. In our previous simulations, with $h/\delta \sim 0.1$, ΔB_1 was comparable to ΔB_2 and ΔB_3, all of order unity. At $\mathrm{Re}_\tau \approx 550$, its value is roughly reduced by two thirds, becoming significantly smaller than the other two terms. Thus, the latter simulations are a more correct representation of real-application conditions, for which ΔB_1 would be negligible.

The term ΔB_2 represents the slip velocity at the riblet tips, and is directly related to the drag-reduction mechanism in the viscous regime,[2,6] remaining proportional to the riblet size over the whole drag-reducing ℓ_g^+ range. When expressed as ΔB_2 instead of DR_2, results at $\mathrm{Re}_\tau \approx 180$ and 550 agree almost exactly, as shown in Figure 7, supporting the universal scaling of ΔB predicted by the theory.

The term ΔB_3 represents the effect of the additional Reynolds stresses in the flow above the riblet tips. Because of the scaling with u_*, the integrand in Eq. (6) differs from zero only near the wall. Figure 7 shows that ΔB_3 is the term responsible for the degradation in performance for riblets larger than $\ell_g^+ \approx 11$, as it increases rapidly for larger sizes, canceling the beneficial effect of ΔB_1 for $\ell_g^+ \approx 20$. ΔB_3 is slightly larger for $\mathrm{Re}_\tau \approx 550$ than for 180, as a direct consequence of the higher intensities found in the $-uv$ cospectrum, portrayed in Figure 5(b). As discussed above, the increase will likely become less significant as Re_τ increases further. Figure 7 also shows the result of evaluating the integrand in Eq. (6) only in the spectral region associated with the spanwise rollers. It shows that this region contains most of the extra stress, roughly 65% for $\mathrm{Re}_\tau \approx 180$ and 75% for $\mathrm{Re}_\tau \approx 550$, reinforcing the conclusion that the rollers are indeed the root cause of the degradation of the drag.

VI. CONCLUSIONS

Results of direct numerical simulations of riblet channels at $\mathrm{Re}_\tau \approx 550$ have been presented, compared with previous results at $\mathrm{Re}_\tau \approx 180$. The difference in Reynolds numbers was sufficient to determine that the spanwise rollers, responsible for the breakdown of performance as riblet size increases, scale in wall units. There is a small increase in the intensity of these structures with the Reynolds number, but it is probably a low-Reynolds-number effect, caused by the growth with Re_τ of the turbulent fluctuations near the wall. This growth is analogous to that in smooth-wall flows, which slows down as Re_τ increases. Although the differences are, again, small, the simulations at $\mathrm{Re}_\tau \approx 550$ are probably more representative of the flow conditions for practical applications. Nevertheless, the present simulations prove that the physical description deduced from the DNSs at $\mathrm{Re}_\tau \approx 180$ was essentially correct, and corroborate the validity of the low-Reynolds-number simulations often found in the literature.

ACKNOWLEDGMENTS

This work was supported in part by the CICYT (Grant No. TRA2009-11498), and by the sixth framework AVERT program of the European Commission, AST5-CT-2006-030914. Ricardo García-Mayoral was partly supported by an FPI fellowship from the Spanish Ministry of Education and Science.

[1] J. Jiménez, "Turbulent flows over rough walls," Ann. Rev. Fluid Mech. **36**, 173–196 (2004).
[2] P. Luchini, F. Manzo, and A. Pozzi, "Resistance of a grooved surface to parallel flow and cross-flow," J. Fluid Mech. **228**, 87–109 (1991).
[3] R. Grüneberger and W. Hage, "Drag characteristics of longitudinal and transverse riblets at low dimensionless spacings," Exp. Fluids **50**, 363–373 (2011).
[4] M. J. Walsh and A. M. Lindemann, "Optimization and application of riblets for turbulent drag reduction," AIAA Paper No. 84–0347, 1984.
[5] D. W. Bechert, M. Bruse, W. Hage, J. G. T. Van der Hoeven, and G. Hoppe, "Experiments on drag-reducing surfaces and their optimization with adjustable geometry," J. Fluid Mech. **338**, 59–87 (1997).
[6] R. García-Mayoral and J. Jiménez, "Hydrodynamic stability and breakdown of the viscous regime over riblets," J. Fluid Mech. **678**, 317–347 (2011).

[7] H. Choi, P. Moin, and J. Kim, "Direct numerical simulation of turbulent flow over riblets," J. Fluid Mech. **255**, 503–539 (1993).
[8] D. C. Chu and G. E. M. Karniadakis, "A direct numerical simulation of laminar and turbulent flow over riblet-mounted surfaces," J. Fluid Mech. **250**, 1–42 (1993).
[9] E. Stalio and E. Nobile, "Direct numerical simulation of heat transfer over riblets," Int. J. Heat Fluid Flow **24**, 356–371 (2003).
[10] O. A. El-Samni, H. H. Chun, and H. S. Yoon, "Drag reduction of turbulent flow over thin rectangular riblets," Int. J. Eng. Sci. **45**, 436–454 (2007).
[11] E. Wassen, R. Grueneberger, F. Kramer, W. Hage, R. Meyer, and F. Thiele, "Turbulent drag reduction by oscillating riblets," in *Proceedings of the 4th AIAA Flow Control Conference* (AIAA, Seattle, WA, 2008).
[12] F. Kramer, R. Grüneberger, F. Thiele, E. Wassen, W. Hage, and R. Meyer, "Wavy riblets for turbulent drag reduction," in *Proceedings of the 5th AIAA Flow Control Conference* (AIAA, Chicago, IL, 2010).
[13] S.-H. Lee and H. J. Sung, "Direct numerical simulation of the turbulent boundary layer over a rod-roughened wall," J. Fluid Mech. **584**, 125–146 (2007).
[14] P. Burattini, S. Leonardi, P. Orlandi, and R. A. Antonia, "Comparison between experiments and direct numerical simulations in a channel flow with roughness on one wall," J. Fluid Mech. **600**, 403–426 (2008).
[15] S. Leonardi and I. P. Castro, "Channel flow over large cube roughness: A direct numerical simulation study," J. Fluid Mech. **651**, 519–539 (2010).
[16] S.-H. Lee, H. J. Sung, and P. A. Krogstad, "Direct numerical simulation of the turbulent boundary layer over a cube-roughened wall," J. Fluid Mech. **669**, 397–431 (2011).
[17] K.-S. Choi, "Near-wall structure of a turbulent boundary layer with riblets," J. Fluid Mech. **208**, 417–458 (1989).
[18] S.-J. Lee and S.-H. Lee, "Flow field analysis of a turbulent boundary layer over a riblet surface," Exp. Fluids **30**, 153–166 (2001).
[19] R. D. Moser, J. Kim, and N. N. Mansour, "Direct numerical simulation of turbulent channel flow up to $\mathrm{Re}_\tau = 590$," Phys. Fluids **11**, 943 (1999).
[20] R. García-Mayoral, "The interaction of riblets with wall-bounded turbulence," Ph.D. dissertation (Universidad Politécnica de Madrid, 2011).
[21] O. Flores and J. Jiménez, "Hierarchy of minimal flow units in the logarithmic layer," Phys. Fluids **22**, 071704-1 (2010).
[22] R. B. Dean, "Reynolds number dependence of skin friction and other bulk variables in two-dimensional rectangular duct flow," J. Fluids Eng. **100**, 215–223 (1978).
[23] F. H. Clauser, "The turbulent boundary layer," Adv. Appl. Mech. **4**, 1–51 (1956).
[24] P. R. Spalart and J. D. McLean, "Drag reduction: Enticing turbulence, and then an industry," Philos. Trans. R. Soc. London, Ser. A **369**, 1556–1569 (2011).
[25] R. García-Mayoral and J. Jiménez, "Drag reduction by riblets," Philos. Trans. R. Soc. London, Ser. A **369**, 1412–1427 (2011).
[26] J. Jiménez, "On the structure and control of near wall turbulence," Phys. Fluids **6**, 944–953 (1994).
[27] S. Hoyas and J. Jiménez, "Reynolds number effects on the Reynolds-stress budgets in turbulent channels," Phys. Fluids **20**, 101511 (2008).
[28] D. B. D. Graaff and J. K. Eaton, "Reynolds-number scaling of the flat-plate turbulent boundary layer," J. Fluid Mech. **422**, 319–346 (2000).
[29] M. M. Metzger and J. C. Klewicki, "Scaling the near-wall axial turbulent stress in the zero pressure gradient boundary layer," Phys. Fluids **13**, 1819–1821 (2001).
[30] R. Mathis, N. Hutchins, and I. Marusic, "Large-scale amplitude modulation of the small-scale structures in turbulent boundary layers," J. Fluid Mech. **628**, 311–337 (2009).
[31] J. Hunt and J. Morrison, "Eddy structure in turbulent boundary layers," Eur. J. Mech. B/Fluids **19**, 673–694 (2000).
[32] J. Jiménez, "Cascades in wall-bounded turbulence," Ann. Rev. Fluid Mech. **44**, 27–45 (2012).
[33] D. B. Goldstein, R. Handler, and L. Sirovich, "Direct numerical simulation of turbulent flow over a modeled riblet covered surface," J. Fluid Mech. **302**, 333–376 (1995).
[34] S. Hoyas and J. Jiménez, "Scaling of the velocity fluctuations in turbulent channels up to $\mathrm{Re}_\tau = 2003$," Phys. Fluids **18**, 011702 (2006).